

Radiative return meets GVMD

Pau Petit Rosàs^{1,*}, Olga Shekhovtsova^{2,†} and William J. Torres Bobadilla^{1,‡}

¹*Department of Mathematical Sciences, University of Liverpool, Liverpool L69 3BX, U.K.*

²*National Science Center KIPT, Kharkov, Ukraine*

We improve the description of pion-photon interactions in the radiative return process $e^+e^- \rightarrow \pi^+\pi^-\gamma$ at the next-to-leading order by including the pion form factor in the Feynman rules. We present a general calculation of the new amplitudes, and provide an implementation easy to interface with any Monte Carlo generator. We incorporate this framework into the event generator **Phokhara** and study several experimental configurations. Overall, we find percent-level effects appearing in angular differential cross section distributions at colliders whose centre-of-mass energies lie near the peak of the pion form factor. By contrast, total cross sections and distributions in charge-even variables show effects only at the permille level, or no visible differences at all. Finally, we compare the new predictions with KLOE measurements of the forward-backward asymmetry in order to assess the predictive power of the modifications.

I. INTRODUCTION

The muon anomalous magnetic moment, $a_\mu = (g - 2)_\mu/2$ has been measured with a remarkable relative precision of 127 ppb [1–3], by the dedicated Fermilab $g - 2$ experiment and its predecessor at Brookhaven National Laboratory. Owing to its sensitivity to quantum effects, a_μ constitutes a stringent test of the Standard Model, and the comparison between theory and experiment has shown a tension for more than a decade [4, 5]. In this context, the hadronic vacuum polarization contributions (HVP) are of particular relevance: they provide a numerically significant contribution and remain a leading source of theoretical uncertainty. Since they are governed by non-perturbative QCD at low energies, they must be obtained either from first principles using lattice QCD, the choice in WP25 [6] for the a_μ theoretical average, through dedicated experiments such as MUonE [7–9], or indirectly through measurements of the $e^+e^- \rightarrow$ hadrons cross section at GeV-scale electron-positron colliders [10–12]. Recent lattice QCD results [13–16] and the energy-scan measurement from the CMD-3 collaboration [17, 18] suggest a total alleviation of the long-standing discrepancy, reducing the previously quoted $\sim 5\sigma$ tension to a $1 - 2\sigma$ agreement. It is therefore crucial to understand the origin of the differences between lattice QCD determinations and those obtained with experiment-based methods, as well as the reason behind the difference between the most recent CMD-3 measurement and previous data driven results.

A central role in this discussion is played by pion-pair production, $e^+e^- \rightarrow \pi^+\pi^-$, which accounts for more than 70% of the HVP contribution to a_μ . The experimental program for this channel is currently

active: new radiative return studies—characterized by the radiative process $e^+e^- \rightarrow \pi^+\pi^-\gamma$ to scan the pair production cross section at different energies—by BaBar [19], Belle II [20], BESIII [21], and KLOE [22–25] are underway, and updated energy-scan results, which rely on measuring the pion pair production channel at different centre of mass energies, for the CMD-3 and SND collaborations are anticipated. The $\pi^+\pi^-$ channel is also the focus of the recent CMD-3 analysis, which introduced, among other elements, a dedicated investigation of the forward-backward asymmetry [26, 27]. These studies underscored the importance of pion compositeness effects, which had been neglected in earlier treatments. In particular, predictions based on the standard $F_\pi \times$ sQED treatment, effectively describing pions as point-like scalar particles, governed by scalar QED (sQED), dressed by a vector form factor (VFF), were found to strongly disagree with the CMD-3 forward-backward asymmetry data.

This discrepancy was resolved by approaches that incorporate the pion vector form factor, F_π , consistently within loop corrections. The first of these was a framework inspired by generalized vector-meson dominance (GVMD), introduced in [26], in which F_π is fitted by a sum of Breit-Wigner functions. Soon after, the FsQED model [27–29] was developed, relying instead on dispersive relations to determine F_π . In both cases, the form factor enters the loop amplitudes in a well-defined manner, thereby eliminating the ambiguity inherent to $F_\pi \times$ sQED regarding the momentum at which F_π should be evaluated. These improved descriptions of the energy-scan channel have been implemented in several Monte Carlo (MC) generators: MCGPJ [30], modified to include GVMD, Babayaga@NLO [31, 32], extended to include both GVMD and FsQED [33], and McMuLe [34], which employs an effective field theory formulation to realize FsQED [35].

Two comments are in order. First, it is worth noting that the GVMD approach employs a parametrization of the pion vector form factor that does not respect

* paupetit@liverpool.ac.uk

† shekhovt@lnf.infn.it

‡ torres@liverpool.ac.uk

analyticity constraints, as it is based on a sum of Breit–Wigner functions. This has no visible impact on the energy scan mode [33].

Second, similar studies have not been done for the radiative return method. In fact, several open issues remain in this channel. They ultimately trace back to the fact that, with current technology, the full Compton tensor cannot be embedded in loop calculations. Furthermore, for the radiative return, it is not known if FsQED or GVMD provide an accurate description of the one-loop contributions which contain $\gamma^*\gamma^* \rightarrow \pi^+\pi^-\gamma$ [36]. Nevertheless, implementing these models for the other diagrams is already a meaningful step that directly improves the theoretical description, while an implementation for all cases might be useful in the future.

We bridge the gap between the energy-scan and radiative return approaches by providing a calculation of the GVMD modifications in a form that is straightforward to interface with any MC generator, providing a **Fortran** implementation in the Ancillary files [37]. Then, to assess the impact of the GVMD corrections in the radiative channel, we implement the code in the widely used MC generator **Phokhara** [38–44], which has been the tool of choice at ϕ - and B -factories for radiative return studies. Finally, we use the new version of **Phokhara** to measure the impact of the GVMD modifications in a set of benchmark scenarios, defined in [36], as well as to compare the MC predictions with KLOE data for the forward–backward asymmetry. In the latter, we remark the importance of additional contributions coming from meson resonances.

This paper is organized as follows. Section II presents the setup of the radiative return process together with a brief overview of the pion-photon interactions, with particular emphasis on the GVMD model. Section III discusses the implementation strategy of the GVMD and the validation of the corrections to the radiative return process. Section IV investigates how the GVMD modifications affect different phenomenological settings, and highlights the nature of the results. The role of these effects is also studied on experimental data. Conclusions summarizing our findings and outlining directions for future work are provided in Section V.

II. THE RADIATIVE RETURN PROCESS

We focus our attention on the radiative return process $e^+(p_1)e^-(p_2) \rightarrow \pi^+(p_3)\pi^-(p_5)\gamma(p_4)$, whose tree-level contribution takes the form,

$$\mathcal{A}^{(0)} = A_{\text{ISR}}^{(0)} + A_{\text{FSR}}^{(0)}, \quad (1)$$

where the subscripts account for the emission of the hard photon from the leptonic lines, initial state radiation (ISR), and from the hadronic lines, final state

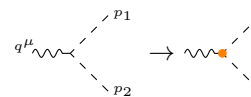
radiation (FSR). One can perform perturbative corrections on the electronic and hadronic contributions. By following the convention of Ref. [36], we respectively refer to them as initial state corrections (ISC) and final state corrections (FSC). For instance, one-loop corrections to the radiative return process can be expressed as,

$$\mathcal{A}^{(1)} = \sum_{\mathcal{X} \in \{\text{ISR}, \text{FSR}\}} A_{\text{ISC};\mathcal{X}}^{(1)} + A_{\text{FSC};\mathcal{X}}^{(1)} + A_{\text{TPE};\mathcal{X}}^{(1)}, \quad (2)$$

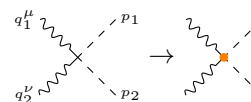
where the TPE term accounts for the two-photon-exchange diagrams. Note that additional vacuum-polarization contributions are included in the definition of the VFF. In the standard $F_\pi \times \text{sQED}$ approach, the pion VFF evaluated at s_{12} multiplies all FSR contributions as calculated with sQED, whereas all ISR contributions are weighted by $F_\pi(s_{35})$, with $s_{ij} = (p_i + p_j)^2$. It is useful to define:

$$\eta(\mathcal{X}) = \begin{cases} s_{35}, & \text{if } \mathcal{X} = \text{ISR}, \\ s_{12}, & \text{if } \mathcal{X} = \text{FSR}. \end{cases} \quad (3)$$

In GVMD, however, the VFF is inserted at the scalar–photon vertices, thereby modifying the standard sQED Feynman rules to:



$$\rightarrow = i Q_\pi (p_1 - p_2)^\mu F_\pi(q^2), \quad (4)$$



$$\rightarrow = 2i Q_\pi^2 g^{\mu\nu} F_\pi(q_1^2) F_\pi(q_2^2).$$

The vertices thus carry, on top of the expected Lorentz structure inherited in sQED, a VFF that depends on the momentum of the photons. If these carry a definite momentum, F_π can be directly evaluated, yielding the usual treatment of $F_\pi \times \text{sQED}$. Nevertheless, for a set of diagrams, the VFF needs to be evaluated for loop momenta. These relevant one-loop diagrams, modified under the GVMD Feynman rules, correspond to the FSC and TPE groups. A representative diagram for each of them is displayed in Fig. 1. We do not modify FSC corrections with GVMD. Overall, the corrections are expected to be small [33, 35, 36], and, at least for scan processes, are well approximated by $F_\pi \times \text{sQED}$ [33]. On the contrary, we do modify the TPE diagrams.

III. THE TPE DIAGRAMS WITHIN GVMD

The TPE contributions can be broken down into $A_{\text{TPE};\text{ISR}}^{(1)}$ and $A_{\text{TPE};\text{FSR}}^{(1)}$ (see Fig. 1). We calculate both under the GVMD modifications. For the first set of diagrams $A_{\text{TPE};\text{ISR}}^{(1)}$, GVMD is a good approximation to the full Compton tensor, $\gamma^*\gamma^* \rightarrow \pi^+\pi^-$,

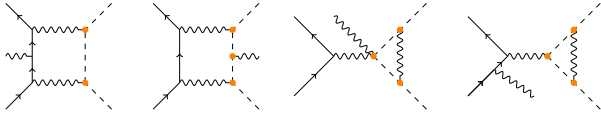


Figure 1: Representative diagrams for the two groups, TPE and FSC, changing under GVMD. The groups are further split into ISR and FSR contributions, corresponding from left to right to TPE_{ISR} , TPE_{FSR} , FSC_{FSR} and FSC_{ISR} .

and is an improvement over the usual $F_\pi \times \text{sQED}$ description. We will also refer to it as GVMD_{ISR} , and always show it by itself in the results of Section IV. It is unclear if GVMD is a valid approximation to describe the other set of diagrams $A_{TPE;FSR}^{(1)}$. As recently shown in the photon soft limit approximation [45], $F_\pi \times \text{sQED}$ is a valid first approximation to the $\gamma^* \gamma^* \gamma \rightarrow \pi^+ \pi^-$ process. Thus, it is plausible that GVMD is also an improvement in this case. Consequently, both as a natural extension to GVMD_{ISR} , and to prepare for the future, we decide to also include $A_{TPE;FSR}^{(1)}$, with the option of turning it on and off left to the user of the code (see Section IV and

$$\begin{aligned}
 \text{GVMD} &= \underbrace{\text{sQED}}_{\delta_{NN}} - \sum_v a_v \left(\underbrace{\text{DEQs}}_{\delta_{MN}(\Lambda_v)} + \underbrace{\text{DEQs}}_{\delta_{MM}(\Lambda_v, \Lambda_w)} \right) + \sum_{v,w} a_v a_w \underbrace{\text{DEQs}}_{\delta_{MM}(\Lambda_v, \Lambda_w)}. \quad (6)
 \end{aligned}$$

The GVMD amplitude of the TPE diagrams is thus easy to write down as,

$$\begin{aligned}
 A_{TPE;\mathcal{X}}^{(1)} &= \delta_{NN}^{\mathcal{X}} \\
 &+ \sum_v a_v \left[\delta_{MN}^{\mathcal{X}}(\Lambda_v) + \sum_w a_w \delta_{MM}^{\mathcal{X}}(\Lambda_v, \Lambda_w) \right]. \quad (7)
 \end{aligned}$$

This works for both $\mathcal{X} \in \{ISR, FSR\}$, and allows one to calculate any general VFF Breit–Wigner fit. It is of interest to note that the GVMD modifications do not introduce ultraviolet (UV) singularities and leave unchanged the infrared (IR) structure of the one-loop contribution predicted by lower $F_\pi \times \text{sQED}$ amplitudes in these diagrams [46]. Specifically, δ_{NN} , δ_{MN} , δ_{MM} are individually UV finite, and the IR divergent singularities come only from δ_{NN} , δ_{MN} , with δ_{MM} a fully finite contribution. Hence, we can split the GVMD

Appendix A for additional details).

We perform the calculation of the amplitudes working in dimensional regularization. Following [26], we parametrize the VFF as a sum of Breit–Wigner terms,

$$F_\pi(q^2) = \sum_v a_v \left(1 + \frac{q^2}{\Lambda_v - q^2} \right), \quad (5)$$

with the constraint that $F_\pi(0) = 1$, and thus the constants a_v need to satisfy $\sum_v a_v = 1$. The complex parameters $\Lambda_v = m_v^2 - im_v \Gamma_v$ are fixed by the mass m_v and width Γ_v of the vector meson v . The complex parameters Λ_v can be treated as effective masses, which will be acquired by the virtual photon of the interaction. In this way, once both VFF are expanded, we can separate the whole amplitude in three individual contributions, namely contributions that contain only massless photons, δ_{NN} , equivalent to the sQED contribution, those that both virtual photons are effectively massive, $\delta_{MM}(\Lambda_v, \Lambda_w)$, and finally the contributions with only one massive photon, $\delta_{MN}(\Lambda_v)$. This decomposition can be depicted diagrammatically, in the $\mathcal{X} = \text{ISR}$ case as,

contribution as¹,

$$\mathcal{A}_{TPE;\mathcal{X}}^{\text{GVMD}} = \delta_{F_\pi \times \text{sQED}}^{\mathcal{X}} + \delta_{\text{FF}}^{\mathcal{X}}, \quad (8)$$

with

$$\begin{aligned}
 \delta_{F_\pi \times \text{sQED}}^{\mathcal{X}} &= F_\pi(\eta(\mathcal{X})) \delta_{NN}^{\mathcal{X}}, \\
 \delta_{\text{FF}}^{\mathcal{X}} &= \sum_v a_v \left[\delta_{MN}^{\mathcal{X}}(\Lambda_v) - \frac{\eta(\mathcal{X})}{\Lambda_v - \eta(\mathcal{X})} \delta_{NN}^{\mathcal{X}} \right. \\
 &\quad \left. + \sum_w a_w \delta_{MM}^{\mathcal{X}}(\Lambda_v, \Lambda_w) \right]. \quad (9)
 \end{aligned}$$

If $\delta_{\text{FF}} = 0$, one easily recovers $F_\pi \times \text{sQED}$. In order to avoid complications related to different regularization schemes in different MC generators, and make

¹ There is a slight abuse in the notation adopted here. Within the GVMD framework, the quantity actually computed corresponds to the interference between the relevant subset of TPE diagrams and the Born amplitude, which introduces factors of $F_\pi^\dagger(\eta(\mathcal{X}))$ from the Born amplitude.

our calculation easy to interface, we provide **Fortran** routines to evaluate δ_{FF} in the ancillary files [37], and give instructions on how to use them in Appendix A. Note that δ_{FF} is defined such that it is IR finite, concentrating the IR structure in $\delta_{F_\pi \times \text{sQED}}$, which automatically matches the real corrections.

The calculation of the amplitudes of δ_{FF} is performed with two different methods, to compare and ensure the correctness of the result. In one, a dedicated pipeline with the combination of **qgraf** [47], **Tapir** [48], and **Form** [49–52] is used to generate, dress and evaluate the topologies, directly with the GVMD Feynman rules, which are implemented in a custom model in **Tapir**. In the other, the needed amplitudes are calculated with **FEYNARTS** [53] and **FEYNCALC** [54]. In this case, instead of modifying the sQED Feynman rules, the groups δ_{MM} and δ_{MN} are obtained from δ_{NN} , by means of a “massification” of the loop propagators, $\mathcal{A}_{\text{TPE}}^{\text{sQED}} \rightarrow \mathcal{A}_{\text{TPE}}^{\text{GVMD}}$, closely following (6). Agreement is found between methods.

In addition, we test two complementary strategies for evaluating the amplitudes. The first strategy employs integration-by-parts (IBP) identities [55, 56], generated with **Kira** [57], to reduce all loop integrals to a set of master integrals [58]. Following the basis suggested by the rotation matrix of the differential equation constructed in [59], we isolate the IR singularity and thereby evaluate the remaining Feynman integrals directly in strictly four space-time dimensions, with **Collier** [60, 61]. The second strategy follows the conventional tensor-integral approach: the one-loop tensor integrals (up to rank 2) are reduced to the standard Passarino–Veltman basis and are likewise evaluated with **Collier**.

Although the IBP reduction substantially decreases the number of integrals, the increased algebraic complexity of the kinematic prefactors generated by the IBP identities leads to an overall worse performance, by roughly a factor of 5, relative to the second strategy. In the latter, the $\mathcal{O}(300)$ scalar integrals dominate the CPU time, while the evaluation of the kinematic coefficients is negligible, especially after further optimization with **Form**.

Finally, we find that organizing the amplitudes into the δ_{NN} , δ_{MN} , and δ_{MM} components reduces CPU time by enabling extensive reuse of **Collier**’s caching: the same loop functions are evaluated repeatedly for different Λ values, rather than recomputing the full amplitude for each choice.

IV. RESULTS

We study the impact of the GVMD modifications for a set of scenarios. To do so, we interface the GVMD code to the MC generator **Phokhara**. With it, we explore and discuss all benchmark scenar-

ios presented in [36]. Then, we will review a relaxed KLOE large angle scenario used to study the forward–backward asymmetry, following the investigations performed in [62]. In order to describe KLOE data in the forward–backward asymmetry scenario, additional contributions are needed. These are described in Subsection IV D, and more in detail in Appendix B. Finally, to eliminate biases from using different parametrizations of F_π , we stick to using the one defined in [26] for all scenarios.

To apply cuts to the scenarios and study a range of differential cross section distributions, we define the kinematic variables θ_γ , θ_\pm , which are the photon and pion angles, the hard photon energy, E_γ , and the pion perpendicular and azimuthal momenta, p_z^\pm , p_\perp^\pm , as well as their invariant mass $M_{\pi\pi}$. They are all defined in accordance with the consensus established in [36]. Furthermore, we give the forward–backward asymmetry a definition such that

$$\mathcal{A}_{\text{FB}}(X, Y) = \frac{\frac{d\sigma}{dX}(Y > 90^\circ) - \frac{d\sigma}{dX}(Y < 90^\circ)}{\frac{d\sigma}{dX}(Y > 90^\circ) + \frac{d\sigma}{dX}(Y < 90^\circ)}, \quad (10)$$

where X account for kinematic variables, and Y must strictly be an angular one.

A. KLOE-like large angle

We test the GVMD modifications in a KLOE-like large angle (LA) scenario. Specifically, we apply the following cuts:

$$\begin{aligned} \sqrt{s} &= 1.02 \text{ GeV}, \quad 50^\circ \leq \theta_\pm \leq 130^\circ, \\ E_\gamma &> 20 \text{ MeV}, \quad 50^\circ \leq \theta_\gamma \leq 130^\circ, \\ |p_z^\pm| &> 90 \text{ MeV} \vee p_\perp^\pm > 160 \text{ MeV}, \\ 0.1 \text{ GeV}^2 &\leq M_{\pi\pi}^2 \leq 0.85 \text{ GeV}^2. \end{aligned} \quad (11)$$

We present the comparison between GVMD and $F_\pi \times \text{sQED}$ in Fig. 2, where we display the differential cross section for the scenario, as plotted versus the invariant mass of the pions, $M_{\pi\pi}$, and $\theta_{\text{avg}} = (\theta_- + \theta_+ + \pi)/2$. We split the GVMD contribution in the total one and GVMD_{ISR} . Sub-percent effects are seen in the invariant mass distributions, with maximum of $\sim 0.3\%$, with no particular trend, and maximal deviation in the edges of the distribution. A larger, at the percent level, divergence is observed in the angular distributions. Even in the full GVMD, which tames the pure GVMD_{ISR} , the corrections reach more than one percent in $\theta_{\text{avg}} = 50^\circ$. As the corrections are asymmetric over the angular distributions, the cross-section, seen in Table I, also differs between approaches, with a difference of roughly 0.2%. Due to the biggest contribution to a_μ^{HVP} being the ρ peak region, we also show in Table II the cross section of the region $0.5 \text{ GeV}^2 < M_{\pi\pi}^2 < 0.7 \text{ GeV}^2$.

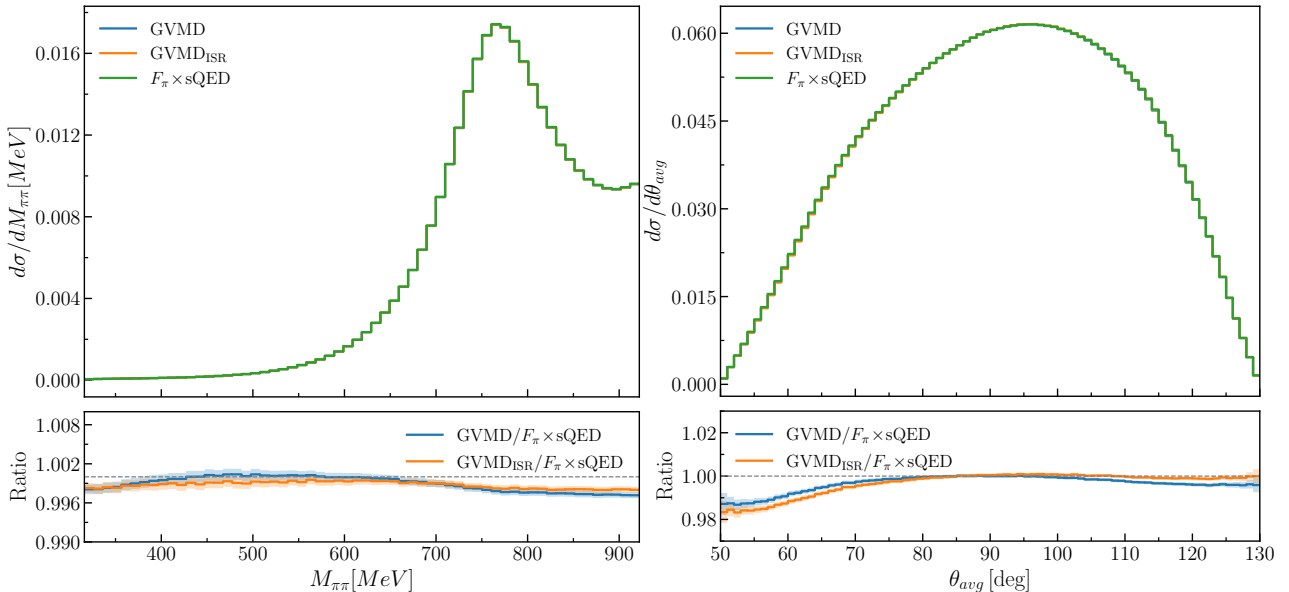


Figure 2: Differential cross section versus pion-pair invariant mass (left) and θ_{avg} (right) under $F_\pi \times sQED$, the full GVMD modifications and only the ISR diagrams modified with GVMD. The bottom panel of each plot shows, the ratio between the modifications and $F_\pi \times sQED$. Colour bands correspond to statistical uncertainties. Note the difference between y-axis scales.

	$\sigma_{F_\pi \times sQED}$	$\sigma_{GVMD_{ISR}}$	σ_{GVMD}
KLOE LA	3.2904(2)	3.2851(2)	3.2839(2)
KLOE SA	16.3046(9)	16.3050(9)	16.3050(9)
BESIII	0.08461(2)	0.08472(2)	0.08473(2)
B	0.010173(4)	0.010175(4)	0.010176(4)

Table I: Cross sections for each scenario as modelled with $F_\pi \times sQED$, GVMD or only the GVMD modifications in ISR contributions. LA and SA denote, respectively, large and small angle scenarios.

	$\sigma_{F_\pi \times sQED}^p$	$\sigma_{GVMD_{ISR}}^p$	σ_{GVMD}^p
KLOE LA	1.9038(2)	1.9010(2)	1.8997(2)
KLOE SA	8.8450(8)	8.8453(8)	8.8452(8)
BESIII	0.03908(1)	0.03915(1)	0.03915(1)
B	0.004747(3)	0.004748(4)	0.004749(3)

Table II: Cross sections for each scenario in the p peak region $0.5 GeV^2 < M_{\pi\pi}^2 < 0.7 GeV^2$ as modelled with $F_\pi \times sQED$, GVMD or $GVMD_{ISR}$. LA and SA denote large and small angle scenarios.

B. KLOE-like small angle

We repeat the analysis for a KLOE-like small angle (SA) scenario. We now apply cuts:

$$\begin{aligned}
 \sqrt{s} &= 1.02 \text{ GeV}, \quad 50^\circ \leq \theta_\pm \leq 130^\circ, \\
 |p_z^\pm| &> 90 \text{ MeV} \quad \vee \quad p_\perp^\pm > 160 \text{ MeV}, \\
 \theta_{\tilde{\gamma}} &\leq 15^\circ \quad \vee \quad \theta_{\tilde{\gamma}} > 165^\circ, \\
 0.35 \text{ GeV}^2 &\leq M_{\pi\pi}^2 \leq 0.95 \text{ GeV}^2,
 \end{aligned} \tag{12}$$

where $\tilde{\gamma}$ represents the polar angle of $\vec{p}_{\tilde{\gamma}} = -(p_+^\vec{p} + p_-^\vec{p})$. The results for the differential cross section distributions are presented in Fig. 3. In this case, GVMD has no observable effect on the invariant mass distribution, nor on any other distribution of a charge-even variable. The angular distributions, however, show a disagreement of roughly the same maximal size as in the large angle scenario, 2%, but with a trend that is symmetric over the phase space. The fact that no deviation is seen in C-even variables, and no impact is observed in the cross section values (also reported in Tables I and II), points towards the main Feynman diagrams contributing to the angular divergence being C-odd. In particular, since the KLOE small angle scenario is dominated by ISR [36], we conjecture that the modifications on the TPE_{ISR} , interfered with $A_{ISR}^{(0)}$, contribute the most. This is supported by the fact that no change is observed between the full GVMD corrections and only the ISR part.

C. BESIII-like and B scenarios

We present here the two remaining scenarios used in the radiative return studies of [36]. Even if they are different scenarios, we group them in the same Subsection for a simple reason. That is, the centre of mass energies of the colliders modelled in these two cases are significantly larger than the energy where F_π peaks. We anticipate that this will greatly minimize the impact of the GVMD modifications, since the pion vector form factor rapidly falls from its peak.

The BESIII experiment runs at $\sqrt{s} = 4 \text{ GeV}$, and we

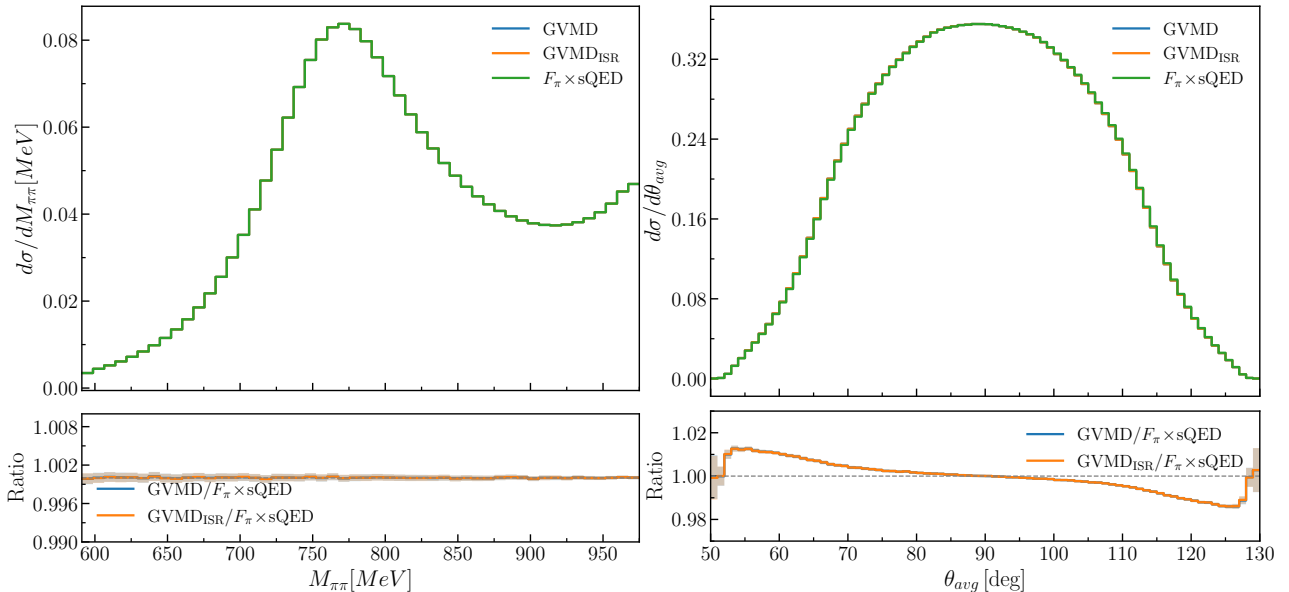


Figure 3: Differential cross section versus pion-pair invariant mass (left) and θ_{avg} (right) under $F_{\pi} \times \text{sQED}$, the full GVMD modifications and only the ISR diagrams modified with GVMD, under the KLOE-like small angle scenario. The ratio between the GVMD modifications and $F_{\pi} \times \text{sQED}$ can be seen in the bottom of the plot.

apply the following cuts for the scenario:

$$\begin{aligned}
 & |\cos \theta_{\pm}| < 0.93 \wedge p_{\pm}^{\perp} > 300 \text{ MeV}, \\
 & ((\cos \theta_{\gamma} < 0.8 \wedge E_{\gamma} > 25 \text{ MeV}) \vee \\
 & (0.86 < |\cos \theta_{\gamma}| < 0.92 \wedge E_{\gamma} > 50 \text{ MeV})), \\
 & \exists! \gamma \text{ with } E_{\gamma} \geq 400 \text{ MeV}.
 \end{aligned} \tag{13}$$

Alternatively, with a centre-of-mass energy roughly an order of magnitude larger than that of KLOE, the B scenario sets $\sqrt{s} = 10 \text{ GeV}$, with experimental cuts for the scenario being:

$$\begin{aligned}
 & 0.65 \text{ rad} \leq \theta_{\pm} \leq 2.75 \text{ rad} \wedge p_{\pm} \geq 1 \text{ GeV}, \\
 & 0.6 \text{ rad} \leq \theta_{\gamma} \leq 2.7 \text{ rad} \wedge E_{\gamma} \geq 3 \text{ GeV}, \\
 & \theta_{\tilde{\gamma}, \gamma^{(h)}} \leq 0.3 \text{ rad}, \quad M_{XX\gamma} \geq 8 \text{ GeV}.
 \end{aligned} \tag{14}$$

We display the differential cross section for each scenario in Fig. 4, as seen versus angular variables. We note that a slight deviation of 0.2% is seen in plots of both angular and charge even variables in the BESIII scenario. This impacts the cross section at the per-mille level (see Table I and Table II). On the contrary, at $\sqrt{s} = 10 \text{ GeV}$ and with cuts from the B scenario, no difference between GVMD and $F_{\pi} \times \text{sQED}$ is seen in any differential cross section distribution nor in the cross section, within the statistical error of the MC.

D. Forward-backward asymmetry

In order to compare the forward-backward asymmetry in KLOE, we use the data from [62].² We run the same scenario, by applying a broad cut on the angle of the charged particles and hard photon, as well as a tight cut on the track mass, such that

$$\begin{aligned}
 & 50^{\circ} \leq \theta_{\gamma, \pm} \leq 130^{\circ}, \\
 & |M_{\text{trk}} - M_{\pm}| < 10 \text{ MeV}.
 \end{aligned} \tag{15}$$

Note that in this case we turn on additional ISC_{FSR} contributions arising from the ϕ decays, which we refer to as ISC_{ϕ} , and discuss in detail in Appendix B. We will always plot them separately with either $F_{\pi} \times \text{sQED}$ or GVMD.

In Fig. 5 we show the KLOE data for the forward-backward asymmetry for both centre of mass energies on-peak (right) and off-peak (left) the ϕ resonance. On top, we display the different MC contributions, that is, only the NLO $F_{\pi} \times \text{sQED}$ corrections, the additional ISC_{ϕ} vector resonances mentioned above, and finally ISC_{ϕ} plus the GVMD_{ISR} and full GVMD modifications. On the middle panels we display the difference between data and approaches, and compare the MC choices on the bottom plots. There are several points to highlight:

1. The additional ISC_{ϕ} contributions are essential to describe KLOE data at $\sqrt{s} = M_{\phi}$. They should also be accounted for in scenarios from Subsection IV A and IV B.

² In particular, we use the preliminary KLOE data presented in Figs. 53 and 54 of Ref [62].

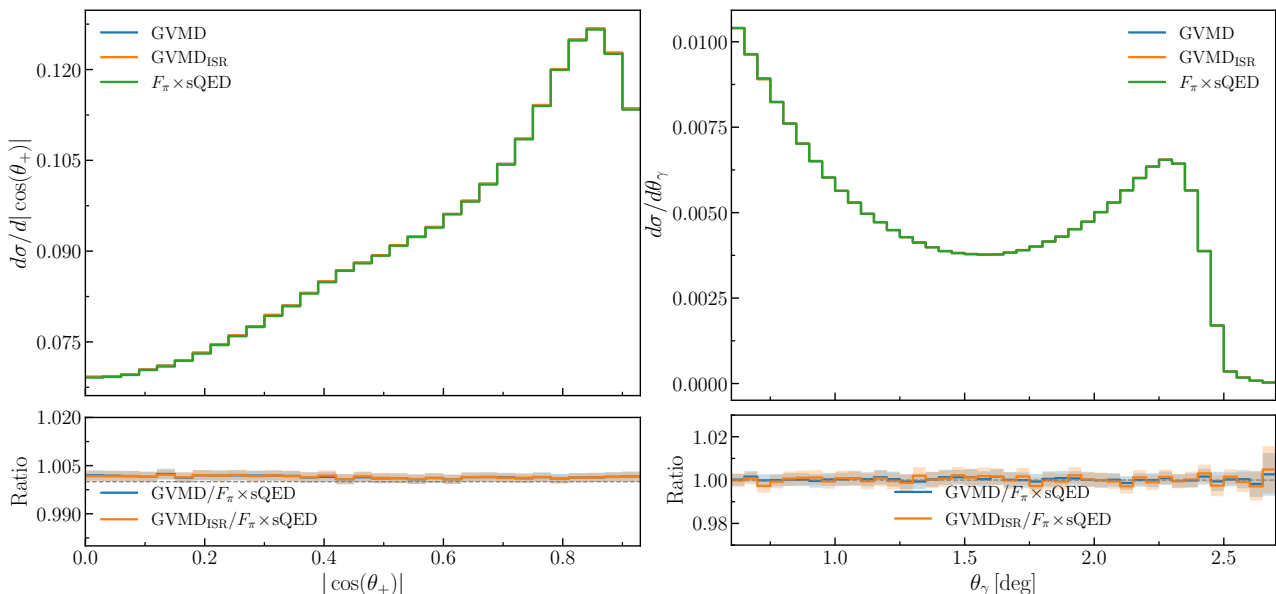


Figure 4: BESIII scenario $|\cos(\theta_+)|$ (left) and B scenario θ_γ (right) differential cross section with the full GVMD modifications, $F_\pi \times s\text{QED}$ and only the ISR diagrams modified with GVMD. The ratio between the approaches is displayed in the bottom panel.

2. All MC models deviate from data at high and low $M_{\pi\pi}^2$, while giving better results in the $0.4 \lesssim M_{\pi\pi}^2 \lesssim 0.8$ window.
3. GVMD does not improve the description of the forward-backward asymmetry within the current experimental accuracy. This is expected to be mitigated with new data being analysed in KLOE-nxt. If we restrict ourselves to the region $0.4 < M_{\pi\pi}^2 < 0.8$, the mean absolute difference between data and ISC_ϕ is $\langle |\Delta_{\text{ISC}_\phi}^{\text{KLOE}}| \rangle = 0.029(2)$, while $\langle |\Delta_{\text{ISC}_\phi + \text{GVMD}}^{\text{KLOE}}| \rangle = 0.025(2)$ for on-peak energies. For $\sqrt{s} = 1$ GeV, $\langle |\Delta_{\text{ISC}}^{\text{KLOE}}| \rangle = 0.037(1)$, while $\langle |\Delta_{\text{ISC} + \text{GVMD}}^{\text{KLOE}}| \rangle = 0.032(1)$. This points towards a slight improvement by considering GVMD, but the conclusion is highly constrained by the precision of the experimental data.
4. In general, differences between MC models are significantly smaller than the difference between data and MC.

Finally, a direct comparison with the energy-scan scenario is not straightforward. In that case, at the ρ peak, \mathcal{A}_{FB} shows a maximal difference between GVMD and $F_\pi \times s\text{QED}$ [26, 27, 33]. Such behavior is not observed in the radiative-return channel. Instead, the forward-backward asymmetry remains close to zero, a feature predicted by both GVMD and $F_\pi \times s\text{QED}$. Overall, the impact of the ρ resonance seems to be tame, and smaller than the effect observed in the energy scan process. A detailed study of the soft photon limit in the amplitudes derived in Eq. (9), as well as the interplay between GVMD and ISC_ϕ corrections, is left for future work.

V. CONCLUSION

This work presented the first implementation of the radiative return process $e^+e^- \rightarrow \pi^+\pi^-\gamma$ at low energies, incorporating an improved description of the non-perturbative pion-photon interaction. The starting point was the point-like approximation of the pion form factor, treated within the factorized $F_\pi \times s\text{QED}$ framework. Building on this, a parametric representation of the Compton tensor in terms of Breit-Wigner functions was introduced, enabling an automated implementation of the non-perturbative dynamics within an inspired GVMD framework. This implementation was designed to be interfaced with Monte Carlo generators relevant for low-energy studies of hadronic cross sections in e^+e^- collisions.

This GVMD implementation was validated within the Monte Carlo generator **Phokhara**, where several phenomenologically relevant scenarios were analysed. We revisited the four benchmark setups introduced in Ref. [36]: two KLOE-like configurations, a BESIII-like selection of experimental cuts, and a setup intended to mimic B -factory conditions. For both KLOE configurations, the GVMD modifications were found to have per-mille or no impact on the total cross section, while percent-level deviations in the angular distributions were observed. Similarly, in the BESIII-like case effects at the level of 0.2% appeared across all distributions. In contrast, no significant deviations were found for the B -factory setup.

As a first step towards validating the descriptive power of GVMD, we have laid the groundwork to pursue the strategy adopted in the energy-scan method, namely to study the forward-backward asymmetry

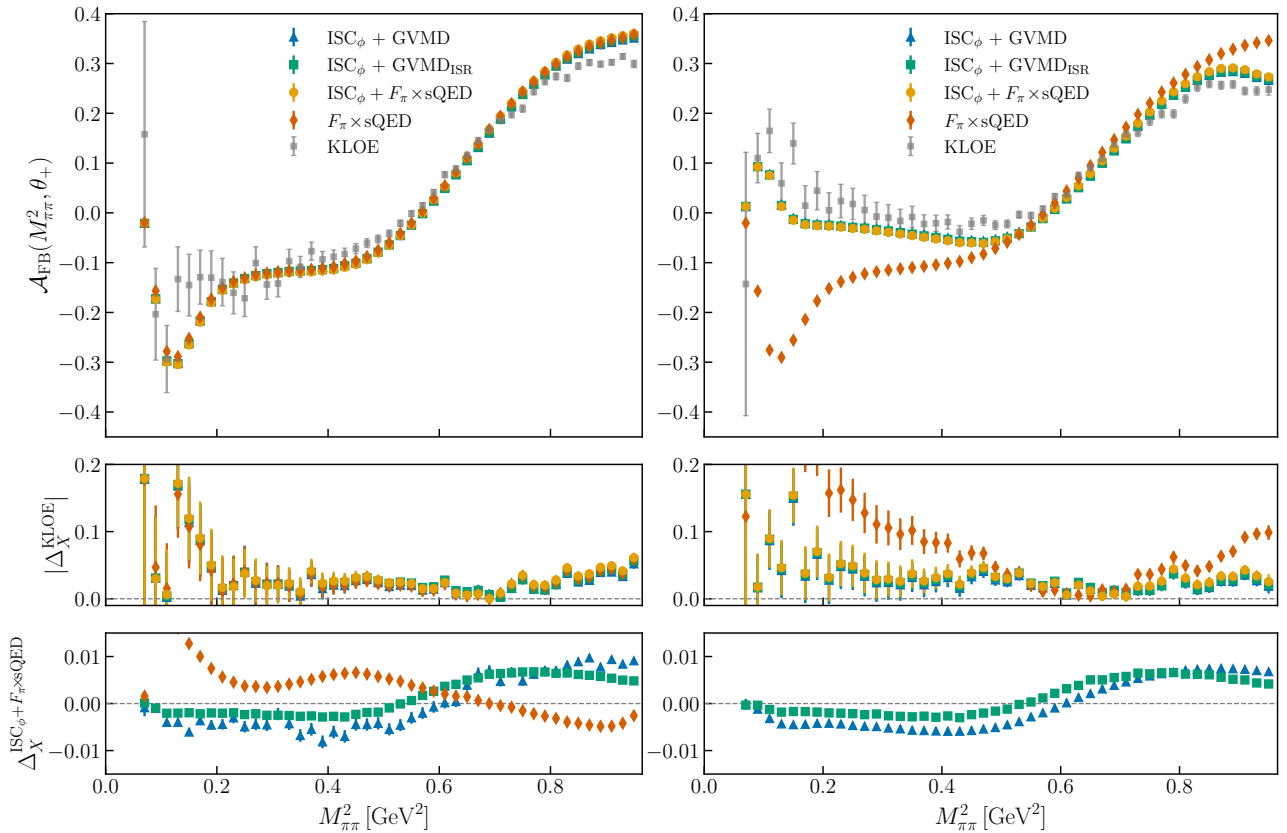


Figure 5: In the top panels we show the forward–backward asymmetry for a relaxed LA KLOE selection at $\sqrt{s} = 1$ GeV (left) and $\sqrt{s} = 1.02$ GeV (right). The KLOE experimental data is shown in grey, while the coloured points correspond to *Phokhara* predictions including different contributions (see text for details). The middle panels display the absolute difference between data and each prediction, $\Delta_X^{KLOE} = KLOE - X$. The bottom panels compare the MC approaches: for the left plot we take $F_\pi \times sQED$ as the reference, while for the right plot we use $F_\pi \times sQED + ISC_\phi$.

and confront the $F_\pi \times sQED$ and GVMD predictions with experimental data. To do so, we have compared the Monte Carlo generator *Phokhara*, upgraded with the new GVMD implementation and the relevant ISC_ϕ meson resonances, with KLOE data, for a broad large-angle scenario and centre of mass energies on and off the ϕ -resonance peak. While definitive conclusions on the predictive power of GVMD were hard to reach due to the large experimental uncertainties, they will be mitigated in the new forthcoming experimental analysis, KLOE-nxt.

Finally, we have provided a code to include the GVMD corrections for the two-photon-exchange channels in any MC event generator. We expect the code, together with ongoing efforts to include FsQED and higher order radiative corrections to improve the overall descriptive power of the MC *Phokhara*.

ACKNOWLEDGMENTS

We are indebted to Fedor Ignatov, Thomas Teubner and Graziano Venanzoni for their unwavering support and for many clarifying discussions since the beginning of this project. We also thank Martin Hoferichter, Fedor Ignatov and Graziano Venanzoni for valuable comments on the manuscript, Stefan Müller for providing the experimental data used in Fig. 5, and Aidan Wright, Thomas Dave and Giovanni Pelliccioli for discussions. This work is supported by the Leverhulme Trust, LIP-2021-014.

Appendix A: Fortran implementation of TPE diagrams within GVMD

We briefly describe the content of the Ancillary files provided in [37], as well as how to employ the Fortran routines provided therein. In particular, we share two main functions, one for $A_{TPE;ISR}^{(1)}$, and one for $A_{TPE;FSR}^{(1)}$, both labeled as $\mathcal{X_GVMD}(\text{ampGVMD}, \text{m12}, \text{m32}, \text{s14}, \text{s15}, \text{s23}, \text{s24}, \text{s35})$, with $\mathcal{X} \in \{ISR, FSR\}$. Both routines work in double precision, with all variables being complex. Each

of the routines take as inputs the initial and final state squared masses, `m12` and `m32`, as well as the kinematic invariants $s_{ij} = (p_i + p_j)^2$, with the momentum configuration described in Section II. They output `ampGVMD`. We exemplify their use by

```
AmpMM $\mathcal{X}$ (ampMM $\mathcal{X}$ ,intsNN $\mathcal{X}$ ,intsMN $\mathcal{X}$ ,intsMM $\mathcal{X}$ ,m12,m32,mpv2,mpw2,s14,s15,s23,s24,s35)
AmpMN $\mathcal{X}$ (ampMN $\mathcal{X}$ ,intsNN $\mathcal{X}$ ,intsMN $\mathcal{X}$ ,m12,m32,mpv2,s14,s15,s23,s24,s35)
```

Note that the user has to provide the values of $F_\pi^\dagger(s_{12})$ and $F_\pi^\dagger(s_{35})$ inside these routines.

The subroutines rely on `IntegralsNN \mathcal{X}` , `IntegralsMN \mathcal{X}` and `IntegralsMM \mathcal{X}` , to calculate the needed vectors of tensor integrals, which have a dedicated cache in `Collier`. They take as input the same kinematic invariants as the `Amp` routines. Furthermore, the kinematic coefficients in the amplitudes are calculated by the `cofMM \mathcal{X}` and `cofMN \mathcal{X}` routines, generated automatically using `Form`'s optimizer.

In total, there are 20 files: two that contain the main routines `mathcal{X}_GVMD`, four more, one for each amplitude to be calculated (two origins from the hard photon times two groups: MM and MN), and four extra for each evaluation of kinematic coefficients. An additional six, one per vector of tensor integrals to evaluate (again, FSR and ISR times NN, MN and MM integrals). The four additional files organize the cache and options of `Collier` (in `modInts.f90`), interface the different routines, `procInterfaces.f90`, compile the example `compile.sh` and finally acts as main, `dFF.f90`.

Appendix B: The ISC_ϕ corrections

At centre-of-mass energies near M_ϕ , corrections from including meson decay processes are large and significant [63–66]. In particular, beyond the FSR part of the ISC related to the $F_\pi \times s\text{QED}$ Bremsstrahlung process,

$$e^+e^- \rightarrow \gamma^* \rightarrow V \rightarrow \pi^+\pi^-\gamma, \quad (\text{B1})$$

the decay via scalar resonance and double resonance processes,

$$\begin{aligned} e^+e^- \rightarrow \gamma^* \rightarrow V \rightarrow S\gamma \rightarrow \pi^+\pi^-\gamma, \\ e^+e^- \rightarrow V_1 \rightarrow (V_2\pi)\gamma \rightarrow \pi^+\pi^-\gamma, \end{aligned} \quad (\text{B2})$$

are large, and need to be taken into account. For the considered energy regions, $S(J^{PC} = 0^{++}) = \{f_0, \sigma\}$ are the possible intermediate scalar mesons leading to the two-pion final state, while only the lowest nonet

applying them to the VFF of Ref. [26], with the parameters of the VFF a_v , and $\Lambda_v = mpv2$, where $v \in \{1, 2, 3\}$. For each combination of vector mesons, one can respectively get `ampMM` = $\delta_{MM}(mpv2, mpw2)$ and `ampMN` = $\delta_{MN}(mpv2) - \frac{x}{mpv2-x}\delta_{NN}$ by calling

of the vector mesons, $V = \{\rho, \omega, \phi\}$, has to be considered.

To account for the resonances (B2), present in the ISC, the Lorentz tensor structure of the decay process $\gamma^* \rightarrow \pi\pi\gamma$, studied in Ref. [67], is elaborated and subsequently incorporated into `Phokhara`, together with the modifications introduced by the GVMD approach. This was previously implemented in the `FASTERD` Monte Carlo generator [63], as well as in an independent version of, `Phokhara 6.1`. It is also worth noting that a related general tensor structure was implemented for the cross-invariant process $\gamma^*\gamma^* \rightarrow \pi\pi$ within a dispersive description of the hadronic light-by-light tensor in Refs. [29, 68].

The processes (B1) and (B2) share the same tensor structure for the hadronic current. In general, the process $\gamma^*(Q) \rightarrow \pi(p_3)\pi(p_5)\gamma(p_4)$, with $Q = p_1 + p_2$ (in absence of ISR) according to the kinematic configuration described in Section II, can be expressed in terms of three independent tensor structures:

$$M_{\gamma^* \rightarrow \pi\pi\gamma}^{\mu\nu} = -ie^2 \sum_{i=1}^3 f_i(Q^2, k \cdot Q, k \cdot l) \tau_i^{\mu\nu}, \quad (\text{B3})$$

with

$$\begin{aligned} \tau_1^{\mu\nu} &= k^\mu Q^\nu - g^{\mu\nu} k \cdot Q, \\ \tau_2^{\mu\nu} &= k \cdot l (l^\mu Q^\nu - g^{\mu\nu} Q \cdot l) + l^\nu (k^\mu Q \cdot l - l^\mu k \cdot Q), \\ \tau_3^{\mu\nu} &= Q^2 (g^{\mu\nu} k \cdot l - k^\mu l^\nu) + Q^\mu (l^\nu k \cdot Q - Q^\nu k \cdot l), \end{aligned} \quad (\text{B4})$$

f_i Lorentz-invariant functions, so called hadronic structure functions, and $l = p_3 - p_5$ and $k = p_4$. The construction of these independent tensor structures makes use of gauge-invariance constraints, together with the transversality and on-shell conditions of the real photon. Further details can be found in Ref. [69].

Because of internal resonances, the total hadronic structure functions are further decomposed as:

$$f_i = f_i^V + f_i^S + f_i^{Br}, \quad i = 1, 2, 3. \quad (\text{B5})$$

Let us emphasise that the decomposition (B3) is model independent; the model dependence resides only in the explicit form of the functions f_i . There is

a wide variety of models for the $\gamma^* \rightarrow S\gamma \rightarrow \pi^+\pi^-\gamma$ production mechanism which differ on the treatment of the scalar mesons and their couplings to the virtual photon [63–66, 70, 71]. In particular, the double-resonance mechanism has been studied within the vector-meson-dominance (VMD) approach and in the more elaborate framework of resonance chiral perturbation theory (R χ PT) in [71, 72].

A detailed comparison of the theoretical model

predictions and the KLOE data for the forward–backward charge asymmetry was presented in [62, 65, 66, 72]. In summary, for on- and off-peak ϕ data, Bremsstrahlung contributions account for the measurements in the 700–900 MeV region, while the inclusion of double-resonance contributions brings the theoretical predictions into agreement with the data at low pion pair invariant mass.

-
- [1] MUON G-2 collaboration, *Measurement of the Positive Muon Anomalous Magnetic Moment to 127 ppb*, *Phys. Rev. Lett.* **135** (2025) 101802 [2506.03069].
- [2] MUON G-2 collaboration, *Measurement of the Positive Muon Anomalous Magnetic Moment to 0.20 ppm*, *Phys. Rev. Lett.* **131** (2023) 161802 [2308.06230].
- [3] MUON G-2 collaboration, *Measurement of the Positive Muon Anomalous Magnetic Moment to 0.46 ppm*, *Phys. Rev. Lett.* **126** (2021) 141801 [2104.03281].
- [4] T. Aoyama et al., *The anomalous magnetic moment of the muon in the Standard Model*, *Phys. Rept.* **887** (2020) 1 [2006.04822].
- [5] T. Blum, A. Denig, I. Logashenko, E. de Rafael, B.L. Roberts, T. Teubner and G. Venanzoni, *The Muon ($g-2$) Theory Value: Present and Future*, **1311.2198**.
- [6] R. Aliberti et al., *The anomalous magnetic moment of the muon in the Standard Model: an update*, *Phys. Rept.* **1143** (2025) 1 [2505.21476].
- [7] C.M. Carloni Calame, M. Passera, L. Trentadue and G. Venanzoni, *A new approach to evaluate the leading hadronic corrections to the muon $g-2$* , *Phys. Lett. B* **746** (2015) 325 [1504.02228].
- [8] MUONE collaboration, *Measuring the leading hadronic contribution to the muon $g-2$ via μe scattering*, *Eur. Phys. J. C* **77** (2017) 139 [1609.08987].
- [9] P. Banerjee et al., *Theory for muon-electron scattering @ 10 ppm: A report of the MUonE theory initiative*, *Eur. Phys. J. C* **80** (2020) 591 [2004.13663].
- [10] A. Keshavarzi, D. Nomura and T. Teubner, *Muon $g-2$ and $\alpha(M_Z^2)$: a new data-based analysis*, *Phys. Rev. D* **97** (2018) 114025 [1802.02995].
- [11] A. Keshavarzi, D. Nomura, T. Teubner and A. Wright, *Muon $g-2$: Blinding for data-driven hadronic vacuum polarization*, *Phys. Rev. D* **111** (2025) L011901 [2409.02827].
- [12] M. Davier, A. Hoecker, B. Malaescu and Z. Zhang, *A new evaluation of the hadronic vacuum polarisation contributions to the muon anomalous magnetic moment and to $\alpha(M_Z^2)$* , *Eur. Phys. J. C* **80** (2020) 241 [1908.00921].
- [13] S. Borsanyi et al., *Leading hadronic contribution to the muon magnetic moment from lattice QCD*, *Nature* **593** (2021) 51 [2002.12347].
- [14] RBC, UKQCD collaboration, *The long-distance window of the hadronic vacuum polarization for the muon $g-2$* , *Phys. Rev. Lett.* **134** (2025) 201901 [2410.20590].
- [15] ETM collaboration, *Strange and charm quark contributions to the muon anomalous magnetic moment in lattice QCD with twisted-mass fermions*, *Phys. Rev. D* **111** (2025) 054502 [2411.08852].
- [16] A. Bazavov et al., *Hadronic vacuum polarization for the muon $g-2$ from lattice QCD: Long-distance and full light-quark connected contribution*, **2412.18491**.
- [17] CMD-3 collaboration, *Measurement of the $e^+e^- \rightarrow \pi^+\pi^-$ cross section from threshold to 1.2 GeV with the CMD-3 detector*, *Phys. Rev. D* **109** (2024) 112002 [2302.08834].
- [18] CMD-3 collaboration, *Measurement of the Pion Form Factor with CMD-3 Detector and its Implication to the Hadronic Contribution to Muon ($g-2$)*, *Phys. Rev. Lett.* **132** (2024) 231903 [2309.12910].
- [19] BABAR collaboration, *Precise Measurement of the $e^+e^- \rightarrow \pi^+\pi^-(\gamma)$ Cross Section with the Initial-State Radiation Method at BABAR*, *Phys. Rev. D* **86** (2012) 032013 [1205.2228].
- [20] BELLE collaboration, *High statistics measurement of the cross-sections of $\gamma\gamma \rightarrow \pi^+\pi^-$ production*, *J. Phys. Soc. Jap.* **76** (2007) 074102 [0704.3538].
- [21] BESIII collaboration, *Measurement of the $e^+e^- \rightarrow \pi^+\pi^-$ cross section between 600 and 900 MeV using initial state radiation*, *Phys. Lett. B* **753** (2016) 629 [1507.08188].
- [22] KLOE collaboration, *Measurement of $\sigma(e^+e^- \rightarrow \pi^+\pi^-\gamma(\gamma))$ and the dipion contribution to the muon anomaly with the KLOE detector*, *Phys. Lett. B* **670** (2009) 285 [0809.3950].
- [23] KLOE collaboration, *Measurement of $\sigma(e^+e^- \rightarrow \pi^+\pi^-)$ from threshold to 0.85 GeV² using Initial State Radiation with the KLOE detector*, *Phys. Lett. B* **700** (2011) 102 [1006.5313].
- [24] KLOE collaboration, *Precision measurement of $\sigma(e^+e^- \rightarrow \pi^+\pi^-\gamma)/\sigma(e^+e^- \rightarrow \mu^+\mu^-\gamma)$ and determination of the $\pi^+\pi^-$ contribution to the muon anomaly with the KLOE detector*, *Phys. Lett. B* **720** (2013) 336 [1212.4524].
- [25] KLOE-2 collaboration, *Combination of KLOE $\sigma(e^+e^- \rightarrow \pi^+\pi^-\gamma(\gamma))$ measurements and determination of $a_\mu^{\pi^+\pi^-}$ in the energy range $0.10 < s < 0.95$ GeV²*, *JHEP* **03** (2018) 173 [1711.03085].
- [26] F. Ignatov and R.N. Lee, *Charge asymmetry in $e^+e^- \rightarrow \pi^+\pi^-$ process*, *Phys. Lett. B* **833** (2022) 137283 [2204.12235].
- [27] G. Colangelo, M. Hoferichter, J. Monnard and J.R. de Elvira, *Radiative corrections to the*

- forward-backward asymmetry in $e^+e^- \rightarrow \pi^+\pi^-$, *JHEP* **08** (2022) 295 [[2207.03495](#)].
- [28] G. Colangelo, M. Hoferichter, M. Procura and P. Stoffer, *Dispersive approach to hadronic light-by-light scattering*, *JHEP* **09** (2014) 091 [[1402.7081](#)].
- [29] G. Colangelo, M. Hoferichter, M. Procura and P. Stoffer, *Dispersion relation for hadronic light-by-light scattering: theoretical foundations*, *JHEP* **09** (2015) 074 [[1506.01386](#)].
- [30] A.B. Arbuzov, G.V. Fedotov, F.V. Ignatov, E.A. Kuraev and A.L. Sibidanov, *Monte-Carlo generator for e^+e^- annihilation into lepton and hadron pairs with precise radiative corrections*, *Eur. Phys. J. C* **46** (2006) 689 [[hep-ph/0504233](#)].
- [31] G. Balossini, C.M. Carloni Calame, G. Montagna, O. Nicrosini and F. Piccinini, *Matching perturbative and parton shower corrections to Bhabha process at flavour factories*, *Nucl. Phys. B* **758** (2006) 227 [[hep-ph/0607181](#)].
- [32] E. Budassi, C.M. Carloni Calame, M. Ghilardi, A. Gurgone, G. Montagna, M. Moretti, O. Nicrosini, F. Piccinini and F.P. Ucci, *Radiative return at NLOPS accuracy*, [2601.19530](#).
- [33] E. Budassi, C.M. Carloni Calame, M. Ghilardi, A. Gurgone, G. Montagna, M. Moretti, O. Nicrosini, F. Piccinini and F.P. Ucci, *Pion pair production in e^+e^- annihilation at next-to-leading order matched to Parton Shower*, *JHEP* **05** (2025) 196 [[2409.03469](#)].
- [34] P. Banerjee, T. Engel, A. Signer and Y. Ulrich, *QED at NNLO with McMule*, *SciPost Phys.* **9** (2020) 027 [[2007.01654](#)].
- [35] Y. Fang, S. Kollatzsch, M. Rocco, A. Signer, Y. Ulrich and M. Zoller, *Disperon QED*, [2512.10709](#).
- [36] R. Aliberti et al., *Radiative corrections and Monte Carlo tools for low-energy hadronic cross sections in e^+e^- collisions*, *SciPost Phys. Comm. Rep.* (2025) 9 [[2410.22882](#)].
- [37] P. Petit Rosàs, O. Shekhovtsova and W.J. Torres Bobadilla, *Ancillary files for “Radiative return meets GVMD”*, [10.5281/zenodo.18881822](#) (2026).
- [38] G. Rodrigo, A. Gehrmann-De Ridder, M. Guillaume and J.H. Kuhn, *NLO QED corrections to ISR in e^+e^- annihilation and the measurement of $\sigma(e^+e^- \rightarrow \text{hadrons})$ using tagged photons*, *Eur. Phys. J. C* **22** (2001) 81 [[hep-ph/0106132](#)].
- [39] G. Rodrigo, H. Czyz, J.H. Kuhn and M. Szopa, *Radiative return at NLO and the measurement of the hadronic cross-section in electron positron annihilation*, *Eur. Phys. J. C* **24** (2002) 71 [[hep-ph/0112184](#)].
- [40] J.H. Kuhn and G. Rodrigo, *The Radiative return at small angles: Virtual corrections*, *Eur. Phys. J. C* **25** (2002) 215 [[hep-ph/0204283](#)].
- [41] H. Czyz, A. Grzelinska, J.H. Kuhn and G. Rodrigo, *The Radiative return at ϕ and B factories: Small angle photon emission at next-to-leading order*, *Eur. Phys. J. C* **27** (2003) 563 [[hep-ph/0212225](#)].
- [42] H. Czyz, A. Grzelinska, J.H. Kuhn and G. Rodrigo, *The Radiative return at ϕ and B factories: FSR at next-to-leading order*, *Eur. Phys. J. C* **33** (2004) 333 [[hep-ph/0308312](#)].
- [43] H. Czyz, P. Kiszka and S. Tracz, *Modeling interactions of photons with pseudoscalar and vector mesons*, *Phys. Rev. D* **97** (2018) 016006 [[1711.00820](#)].
- [44] F. Campanario, H. Czyz, J. Gluza, T. Jeliński, G. Rodrigo, S. Tracz and D. Zhuridov, *Standard model radiative corrections in the pion form factor measurements do not explain the a_μ anomaly*, *Phys. Rev. D* **100** (2019) 076004 [[1903.10197](#)].
- [45] E. Kaziukenas, *Dispersive definition of $\gamma^*\gamma^*\gamma \rightarrow \pi^+\pi^-$ for muon $g-2$ applications*, in *RadioMonteCarLow 2 Satellite 2025*, 2025.
- [46] S. Catani, S. Dittmaier and Z. Trocsanyi, *One loop singular behavior of QCD and SUSY QCD amplitudes with massive partons*, *Phys. Lett. B* **500** (2001) 149 [[hep-ph/0011222](#)].
- [47] P. Nogueira, *Automatic Feynman Graph Generation*, *J. Comput. Phys.* **105** (1993) 279.
- [48] M. Gerlach, F. Herren and M. Lang, *tapir: A tool for topologies, amplitudes, partial fraction decomposition and input for reductions*, *Comput. Phys. Commun.* **282** (2023) 108544 [[2201.05618](#)].
- [49] J.A.M. Vermaseren, *New features of FORM*, [math-ph/0010025](#).
- [50] B. Ruijl, T. Ueda and J. Vermaseren, *FORM version 4.2*, [1707.06453](#).
- [51] J. Kuipers, T. Ueda, J.A.M. Vermaseren and J. Vollinga, *FORM version 4.0*, *Comput. Phys. Commun.* **184** (2013) 1453 [[1203.6543](#)].
- [52] J. Davies, T. Kaneko, C. Marinissen, T. Ueda and J.A.M. Vermaseren, *FORM Version 5.0*, [2601.19982](#).
- [53] T. Hahn, *Generating Feynman diagrams and amplitudes with FeynArts 3*, *Comput. Phys. Commun.* **140** (2001) 418 [[hep-ph/0012260](#)].
- [54] V. Shtabovenko, *FeynCalc 10.2 and FeynHelpers 2: Multiloop calculations streamlined*, [2512.19858](#).
- [55] F.V. Tkachov, *A theorem on analytical calculability of 4-loop renormalization group functions*, *Phys. Lett. B* **100** (1981) 65.
- [56] K.G. Chetyrkin and F.V. Tkachov, *Integration by parts: The algorithm to calculate β -functions in 4 loops*, *Nucl. Phys. B* **192** (1981) 159.
- [57] J. Klappert, F. Lange, P. Maierhöfer and J. Usovitsch, *Integral reduction with Kira 2.0 and finite field methods*, *Comput. Phys. Commun.* **266** (2021) 108024 [[2008.06494](#)].
- [58] S. Laporta, *High-precision calculation of multiloop Feynman integrals by difference equations*, *Int. J. Mod. Phys. A* **15** (2000) 5087 [[hep-ph/0102033](#)].
- [59] P. Petit Rosàs and W.J. Torres Bobadilla, *Fast evaluation of Feynman integrals for Monte Carlo generators*, *JHEP* **09** (2025) 210 [[2507.12548](#)].
- [60] A. Denner and S. Dittmaier, *Reduction of one loop tensor five point integrals*, *Nucl. Phys. B* **658** (2003) 175 [[hep-ph/0212259](#)].
- [61] A. Denner, S. Dittmaier and L. Hofer, *Collier: a fortran-based Complex One-Loop Library in Extended Regularizations*, *Comput. Phys. Commun.* **212** (2017) 220 [[1604.06792](#)].
- [62] WORKING GROUP ON RADIATIVE CORRECTIONS, MONTE CARLO GENERATORS FOR LOW ENERGIES collaboration, *Quest for precision in hadronic cross sections at low energy: Monte Carlo tools vs. experimental data*, *Eur. Phys. J. C* **66** (2010) 585 [[0912.0749](#)].

- [63] O. Shekhovtsova, G. Venanzoni and G. Pancheri, *FASTERD: A Monte Carlo event generator for the study of final state radiation in the process $e^+e^- \rightarrow \pi^+\pi^-\gamma$ at DAPHNE*, *Comput. Phys. Commun.* **180** (2009) 1206 [0901.4440].
- [64] B. Moussallam, *Unified dispersive approach to real and virtual photon-photon scattering at low energy*, *Eur. Phys. J. C* **73** (2013) 2539 [1305.3143].
- [65] L. Roca and E. Oset, *Asymmetry observables in $e^+e^- \rightarrow \pi^+\pi^-\gamma$ in the phi region within a chiral unitary approach*, *Phys. Rev. D* **81** (2010) 014010 [0911.0994].
- [66] A. Gallegos, J.L. Lucio, G. Moreno and M. Napsuciale, *Charge asymmetries in $e^+e^- \rightarrow \pi^+\pi^-\gamma$ at the phi resonance*, *Phys. Lett. B* **693** (2010) 467 [0908.2192].
- [67] S. Dubinsky, A. Korchin, N. Merenkov, G. Pancheri and O. Shekhovtsova, *Final-state radiation in electron-positron annihilation into a pion pair*, *Eur. Phys. J. C* **40** (2005) 41 [hep-ph/0411113].
- [68] M. Hoferichter and P. Stoffer, *Dispersion relations for $\gamma^*\gamma^* \rightarrow \pi\pi$: helicity amplitudes, subtractions, and anomalous thresholds*, *JHEP* **07** (2019) 073 [1905.13198].
- [69] D. Drechsel, G. Knochlein, A. Metz and S. Scherer, *Generalized polarizabilities and the spin averaged amplitude in virtual Compton scattering off the nucleon*, *Phys. Rev. C* **55** (1997) 424 [nucl-th/9608061].
- [70] N.N. Achasov and V.V. Gubin, *Interference in the reaction $e^+e^- \rightarrow \pi^+\pi^-\gamma$ and the final state interaction*, *Phys. Rev. D* **57** (1998) 1987 [hep-ph/9706363].
- [71] G. Isidori, L. Maiani, M. Nicolaci and S. Pacetti, *The $e^+e^- \rightarrow P(1)P(2)$ gamma processes close to the Phi peak: Toward a model-independent analysis*, *JHEP* **05** (2006) 049 [hep-ph/0603241].
- [72] G. Pancheri, O. Shekhovtsova and G. Venanzoni, *Final state radiation and a possibility to test a pion-photon interaction model near two-pion threshold*, *J. Exp. Theor. Phys.* **106** (2008) 470 [0706.3027].